



# Constructing highly active zeolite encapsulated PdAg alloy catalysts for typical VOCs deep oxidation: The role of electron-structure interaction

Qiuli Zhang<sup>a,c,1</sup>, Gan Li<sup>b,1</sup>, Wenming Liu<sup>a,1</sup>, Guobo Li<sup>b</sup>, Tianyao He<sup>b</sup>, Hongxiang Zhang<sup>b</sup>, Yunbo Yu<sup>a,c</sup>, Honggen Peng<sup>a,b,\*</sup>

<sup>a</sup> School of Chemistry and Chemical Engineering, Nanchang University, 999 Xuefu Road, Nanchang, Jiangxi 330031, China

<sup>b</sup> School of Resources and Environment, Nanchang University, 999 Xuefu Road, Nanchang, Jiangxi 330031, China

<sup>c</sup> Ganjiang Innovation Academy, Chinese Academy of Sciences, Ganzhou 341000, China

## ARTICLE INFO

### Keywords:

Elimination of VOCs  
Toluene deep oxidation  
PdAg alloy  
Zeolite encapsulation  
Degradation mechanism

## ABSTRACT

Benzene series volatile organic compounds (VOCs) are extremely toxic and hazardous to human beings and the environment, and their efficient degradation at low temperatures has attracted much attention. Precious metal catalysts are generally recognized as highly active for VOCs removal. Currently, encapsulation of precious metals is an effective strategy to address the lack of long-term stable performance and activity of supported precious metal catalysts. In this work, a PdAg alloy catalyst was successfully constructed inside Slicite-1 (S-1) zeolite (PdAg@S-1) and applied to toluene degradation. The PdAg@S-1 exhibits excellent toluene degradation activity ( $T_{90} = 179^\circ\text{C}$ ) and favorable long-term stability and resistance. The XPS and XAFS results reveal the existence of electronic interactions between Pd and Ag, and the transfer of electrons from Ag to Pd created electron-rich Pd sites. Furthermore, the DFT calculations corroborate that the unique electronic-structural interactions between the PdAg alloys favor the dissociation of the C-H bond and the strong adsorption of gas-phase oxygen, which is the key to the deep oxidation of toluene. The in situ DRIFTS results demonstrate that the reaction followed the Langmuir-Hinshelwood (L-H) mechanism and gas-phase oxygen participates in the redox reaction as an active oxygen species. The construction of high-performance PdAg alloy catalysts by a simple and feasible method inspires the development of catalysts for the efficient degradation of VOCs.

## 1. Introduction

The benzene series of volatile organic compounds (VOCs), which primarily originate from printing inks, adhesives, and manufacturing industries, are extremely toxic and have a high potential for generating total ozone. They pose carcinogenic and teratogenic risks to humans, making the effective degradation of the benzene series an urgent matter. At present, multiple control technologies (adsorption, absorption, biodegradation, thermal incineration, catalytic oxidation, etc.) have been developed to achieve the degradation of VOCs from the source or endpoints [1–4]. Catalytic oxidation, as one of the end-control technologies, can efficiently convert VOCs into harmless  $\text{H}_2\text{O}$  and  $\text{CO}_2$  through heterogeneous catalytic reactions. Additionally, low operating temperatures also allow the technology to be widely applied [5,6]. The key to catalytic oxidation technology lies in the design of efficient, economical, and environmentally friendly catalysts. To date, the

primary catalysts used for VOCs degradation are noble metal-based catalysts and transition metal oxide catalysts [7,8]. Precious metal (Pd, Pt, Rh, Ru, etc.) catalysts exhibit high catalytic activity, enabling for the complete combustion of VOCs at low temperatures. Palladium is extensively utilized in catalysis for hydrogenation reactions [9,10], catalytic oxidation of low-carbon alkanes [11], and catalytic degradation of aromatic hydrocarbons [12], but its practical application is challenged by high cost.

The presence of carriers can enhance the dispersion of active sites, thereby increasing the utilization of precious metals and improving the degradation efficiency of catalysts [13]. Active metal oxides ( $\text{CeO}_2$ ,  $\text{Co}_3\text{O}_4$ ,  $\text{MnO}_2$ ) and inert  $\text{SiO}_2$ ,  $\text{Al}_2\text{O}_3$ , zeolites are commonly adopted as carriers for precious metal catalysts [14–17]. Zeolites have well-defined pore structures, large specific surface area and tunable acidic sites, in particular, the excellent hydrothermal stability makes zeolites widely adopted as support materials for solid catalysts or metal nanoparticles

\* Corresponding author at: School of Chemistry and Chemical Engineering, Nanchang University, 999 Xuefu Road, Nanchang, Jiangxi 330031, China.

E-mail address: [penghonggen@ncu.edu.cn](mailto:penghonggen@ncu.edu.cn) (H. Peng).

<sup>1</sup> These authors contributed equally to this work.

[18]. However, supported catalysts may experience migration and Ostwald ripening of precious metals during prolonged catalytic reactions, leading to sintering and deactivation of the metal [19,20]. The development of metal@zeolite encapsulated catalysts offers a viable solution to mitigate the propensity of precious metals to aggregate. The rigid skeleton and well-defined pore structure inside zeolite enable the encapsulation of precious metal particles, effectively preventing their agglomeration.

It has been reported that the introduction of another metal M (Ag, Au, Cu, Pt, Ni, etc.) into Pd nanomaterials to construct Pd-M alloys can optimize the performance of Pd-based catalyst. Xie et al. [21] reported that three-dimensionally ordered macroporous (3DOM)  $\text{Mn}_2\text{O}_3$ -supported PdAu alloy catalyst could promote oxygen adsorption activation and improve toluene degradation activity and hydrothermal stability. Metal Ag, as a common sacrificial agent, often exists in the form of PdAg alloy structure when coexisting with metal Pd, and the synergistic effect between PdAg has been widely investigated. Liu et al. [22] found that alloyed PdAg/ $\text{Fe}_2\text{O}_3$  catalysts, which showed superior cyclohexane combustion performance and higher stability. Coincidentally, Song et al. [23] also reported that PdAg alloy loading on Ti-SBA-15 carriers could increase the Lewis and Bronsted acid sites of the catalysts, promoting cyclohexane degradation activity and improving stability. Alloying is a powerful way to enhance metal-carrier interactions and improve catalytic performance.

Herein, the Silicalite-1 (S-1) zeolite-encapsulated nanoscale PdAg alloy catalyst (PdAg@S-1) was successfully prepared by a facile one-pot hydrothermal method and displayed excellent toluene combustion performance ( $T_{90}=179^\circ\text{C}$ ). Notably, anchoring of precious metals by the pore structure of zeolites inhibits sintering aggregation of active ingredients, enabling the catalyst to demonstrate exceptional toluene catalytic oxidation activity even under prolonged exposure to harsh conditions. The physicochemical properties and microelectronic environment of the catalysts were investigated by X-ray diffraction (XRD), transmission electron microscopy (TEM) and X-ray photoelectron spectroscopy (XPS). In situ diffuse reflectance infrared Fourier transform spectroscopy (In situ DRIFTS) and density functional theory (DFT) calculations were employed to further reveal the degradation mechanism of toluene over the PdAg@S-1 catalyst. The activation of gas-phase oxygen by the PdAg alloying sites accelerated the deep mineralization of toluene. This work provides some important information to gain insight into the role of alloy composition in the catalytic oxidation of aromatic hydrocarbons and offers a new perspective on the deep oxidation of VOCs.

## 2. Experimental section

### 2.1. Catalyst preparation

#### 2.1.1. Synthesis of pure Silicalite-1 (S-1)

The pure S-1 support was prepared by the one-pot hydrothermal method. First, 15.5 g of deionized water and 13.0 g of tetrapropylammonium hydroxide (TPAOH, 25 wt%) solution were mixed and stirred for 20 min, then 8.32 g of tetraethyl orthosilicate (TEOS, 98 wt%) solution was added and stirred for 6 h at room temperature to obtain a molar ratio of  $\text{SiO}_2$ : TPAOH: water = 1: 0.4: 35 of the clear mixture. Finally, the mixture was transferred into a 100 mL teflon-lined stainless steel autoclave, and crystallized for 3 d under static conditions of  $170^\circ\text{C}$ . The obtained solid products are washed 2–3 times with deionized water and ethanol absolute, respectively, dried overnight in an oven at  $80^\circ\text{C}$ , and then calcined for 4 h at  $500^\circ\text{C}$  in an air atmosphere to remove the organic template.

#### 2.1.2. Synthesis of Pd@S-1, Ag@S-1, PdAg@S-1

Before synthesizing the three catalysts, 0.068 g  $[\text{Pd}(\text{NH}_3)_4](\text{NO}_3)_2$ , 0.038 g  $\text{AgNO}_3$ , 0.041 g  $[\text{Pd}(\text{NH}_3)_4](\text{NO}_3)_2$  and 0.015 g  $\text{AgNO}_3$  mixture were dissolved in 4 mL of deionized water, respectively. After the solid

was completely dissolved, 1 mL of ethylenediamine solution was added to the aqueous solution containing different types of metals and sonicated for 30 min for use. Secondly, the synthesis of Pd@S-1, Ag@S-1, and PdAg@S-1 are similar to the synthesis of pure S-1, the difference is that after adding the calculated amount of TEOS and stirring for 5 h, the corresponding above-mentioned mixed solutions were slowly added respectively, and the stirring was continued for 1 h. Finally, the mixture was transferred to a 100 mL teflon-lined stainless steel autoclave and crystallized in an oven at  $170^\circ\text{C}$  for 3 d. The subsequent processing is the same as that of S-1, the solid product was washed 2–3 times with deionized water and ethanol absolute, respectively, and then placed in an oven at  $80^\circ\text{C}$  for overnight drying. After roasting at  $500^\circ\text{C}$  for 4 h, Pd@S-1, Ag@S-1 and PdAg@S-1 solid products were obtained respectively.

#### 2.1.3. Synthesis of PdAg/S-1

The PdAg/S-1 catalyst was synthesized by wet impregnation. First, 2 g of uncalcined pure S-1 support was placed in a 25 mL beaker, and then 4 mL of an aqueous solution containing the calculated amounts of  $[\text{Pd}(\text{NH}_3)_4](\text{NO}_3)_2$  and  $\text{AgNO}_3$  was added to the beaker, after stirring at room temperature for 6 h, the mixture was dried in an oven at  $80^\circ\text{C}$ , and calcined in air at a heating rate of  $2^\circ\text{C}/\text{min}$  to  $500^\circ\text{C}$  for 4 h. Finally, the PdAg/S-1 sample was obtained.

### 2.2. Catalyst characterization

The prepared catalysts were characterized by different means, including X-ray diffraction (XRD), inductively coupled plasma optical emission spectroscopy (ICP-OES), transmission electron microscopy (TEM), aberration-corrected high-angle annular dark-field TEM (AC-HAADF-TEM),  $\text{N}_2$  adsorption-desorption (BET), X-ray photoelectron spectroscopy (XPS), CO-temperature programmed desorption (CO-TPD),  $\text{O}_2$ -temperature-programmed desorption ( $\text{O}_2$ -TPD),  $\text{H}_2$  temperature-programmed reduction ( $\text{H}_2$ -TPR), Pd K-edge and Ag K-edge X-ray absorption fine structure (XAFS) spectra, in situ diffuse reflectance infrared Fourier transform spectroscopy (in situ DRIFTS) and density functional theory (DFT) were also performed to explore the reaction mechanism of toluene on catalysts. The detailed characterization procedures were presented in [Supporting Information](#).

### 2.3. Catalytic activity evaluation

The synthesized catalysts were all reduced at  $400^\circ\text{C}$  for 2 h in a 10%  $\text{H}_2/\text{Ar}$  atmosphere before evaluating the performance of the catalysts for toluene degradation. 90 mg of catalyst (40–60 mesh) was put into a quartz tubular fixed-bed reactor, and both ends of the catalyst were filled with a small amount of quartz wool. The catalytic oxidation activity of the catalysts for toluene was assessed in a 1000 ppm  $\text{C}_7\text{H}_8/\text{Air}$  atmosphere over a temperature range of  $80$ – $280^\circ\text{C}$ , ramping up at a rate of  $4^\circ\text{C}/\text{min}$ . A feed gas of 1000 ppm  $\text{C}_7\text{H}_8/\text{Air}$  was generated by air bubbling. The total gas flow rate was  $30\text{ mL}\cdot\text{min}^{-1}$  and the weight hourly space velocity (WHSV) was fixed at  $20000\text{ mL}\cdot\text{g}_{\text{cat}}^{-1}\cdot\text{h}^{-1}$ . Finally, the reactants and products were monitored through an online gas chromatograph (GC-7900) that was equipped with a flame ionization detector (FID), whereas  $\text{CO}_2$  was detected with a TCD detector. The  $\text{C}_7\text{H}_8$  conversion ( $X_{\text{C}_7\text{H}_8}$ ),  $\text{CO}_2$  yield ( $Y_{\text{CO}_2}$ ) and  $\text{CO}_2$  selectivity ( $S_{\text{CO}_2}$ ) were calculated according to the following equation:

$$X_{\text{C}_7\text{H}_8}(\%) = \frac{[\text{C}_7\text{H}_8]_{\text{in}} - [\text{C}_7\text{H}_8]_{\text{out}}}{[\text{C}_7\text{H}_8]_{\text{in}}} \times 100$$

$$Y_{\text{CO}_2}(\%) = \frac{[\text{CO}_2]}{[\text{C}_7\text{H}_8]_{\text{in}} \times 7} \times 100$$

$$S_{\text{CO}_2}(\%) = \frac{[\text{CO}_2]_{\text{out}}}{[\text{C}_7\text{H}_8]_{\text{in}} \times X_{\text{C}_7\text{H}_8} \times 7} \times 100$$

where the  $[C_7H_8]_{in}$  and  $[C_7H_8]_{out}$  express the inlet and outlet  $C_7H_8$  concentration (ppm) in the feed stream,  $[CO_2]_{out}$  is the outlet concentration (ppm) of  $CO_2$ .

When the conversion of toluene was below 15%, kinetic experiments for the toluene degradation reaction were conducted for each catalyst. First, 30 mg of catalyst and 120 mg of inert quartz sand (40–60 mesh) were mixed uniformly and put into a quartz tube. Both ends of the well-mixed catalyst and quartz sand were filled with a small amount of quartz wool to fix the mixture. Tests were performed in a feed gas atmosphere of 1000 ppm  $C_7H_8$ /Air at a flow rate of  $50 \text{ mL} \cdot \text{min}^{-1}$  (WHSV =  $100,000 \text{ mL} \cdot \text{g}_{cat}^{-1} \cdot \text{h}^{-1}$ ), eliminating the effects of internal and external diffusion (details of the process are listed in the [Supporting Information](#)). The reaction rate ( $r_{C_7H_8}$ ,  $\text{mol} \cdot \text{g}^{-1} \cdot \text{s}^{-1}$ ) and turnover frequency (TOF,  $\text{s}^{-1}$ ) are calculated according to the following equations:

$$r_{C_7H_8} = X_{C_7H_8} \cdot V_{C_7H_8} / g_{cat}$$

$$TOF = X_{C_7H_8} \cdot V_{C_7H_8} \cdot \frac{M_{metal}}{m_{cat} \omega_{metal} D_{metal}}$$

where  $V_{C_7H_8}$  is the gas flow rate of toluene ( $\text{mol} \cdot \text{s}^{-1}$ ),  $g_{cat}$  is the weight of catalyst (g),  $M_{metal}$  is the molar mass of the metal ( $\text{g} \cdot \text{mol}^{-1}$ ),  $m_{cat}$  is the mass of the catalyst (g),  $\omega_{metal}$  is the mass fraction of the metal (measured by ICP),  $D_{metal}$  is the dispersion of the metal (measured by CO-TPD).

#### 2.4. DFT calculations

All calculations were based on the first principles of DFT, carried out in the Vienna ab-initio simulation package, and the adsorption energy of toluene molecules adsorbed on the surface of the PdAg@S-1 catalyst was calculated according to the following equation:

$$E_{ads} = E_c - (E_T + E_S)$$

where  $E_c$  is the energy of the sample surface and adsorption complex,  $E_T$  is the energy of the isolated adsorbate, and  $E_S$  is the energy of cleaning the sample surface. Detailed information on the calculation can be obtained from the [Supporting Information](#).

### 3. Results and discussion

#### 3.1. Crystalline structures and formation of alloying species

The XRD comparison patterns of various catalysts after reduction are presented in [Fig. S1](#). The characteristic diffraction peaks associated with the MFI structure were observed in all catalysts. Additionally, diffraction peaks corresponding to the crystal faces of Pd (111) and Ag (111) were detected at  $2\theta = 40.11$  and  $38.10^\circ$  in the Pd@S-1 and Ag@S-1 catalysts, respectively, suggesting that the metal Pd and Ag underwent partial migrated and aggregated during the reduction or calcination process. However, no diffraction peaks related to Pd and Ag species were observed in the PdAg@S-1 and supported PdAg/S-1 catalysts, revealing that the coexistence of two metals can maintain a highly dispersed under harsh conditions. Next, the micromorphological structures of the catalysts were explored by TEM images, as depicted in [Fig. S2-S5](#). The prepared catalysts all possessed a regular morphology structure, and the average particle sizes of metal Pd and Ag in the Pd@S-1 and Ag@S-1 catalysts were 1.9 and 4.9 nm, respectively, indicating that the metal Ag tends to aggregate more easily. Notably, the average particle size of metal in the PdAg@S-1 catalyst encapsulating bimetallic compositions was slightly increased (2.0 nm) compared to that of the Pd@S-1 catalyst (1.9 nm), and thus it is hypothesized that an abundant PdAg alloy was formed in this sample, which led to a slight increase in its particle size. In [Fig. 1e](#), the d spacing of the fcc Pd (111) and fcc Ag (111) phases is 0.22

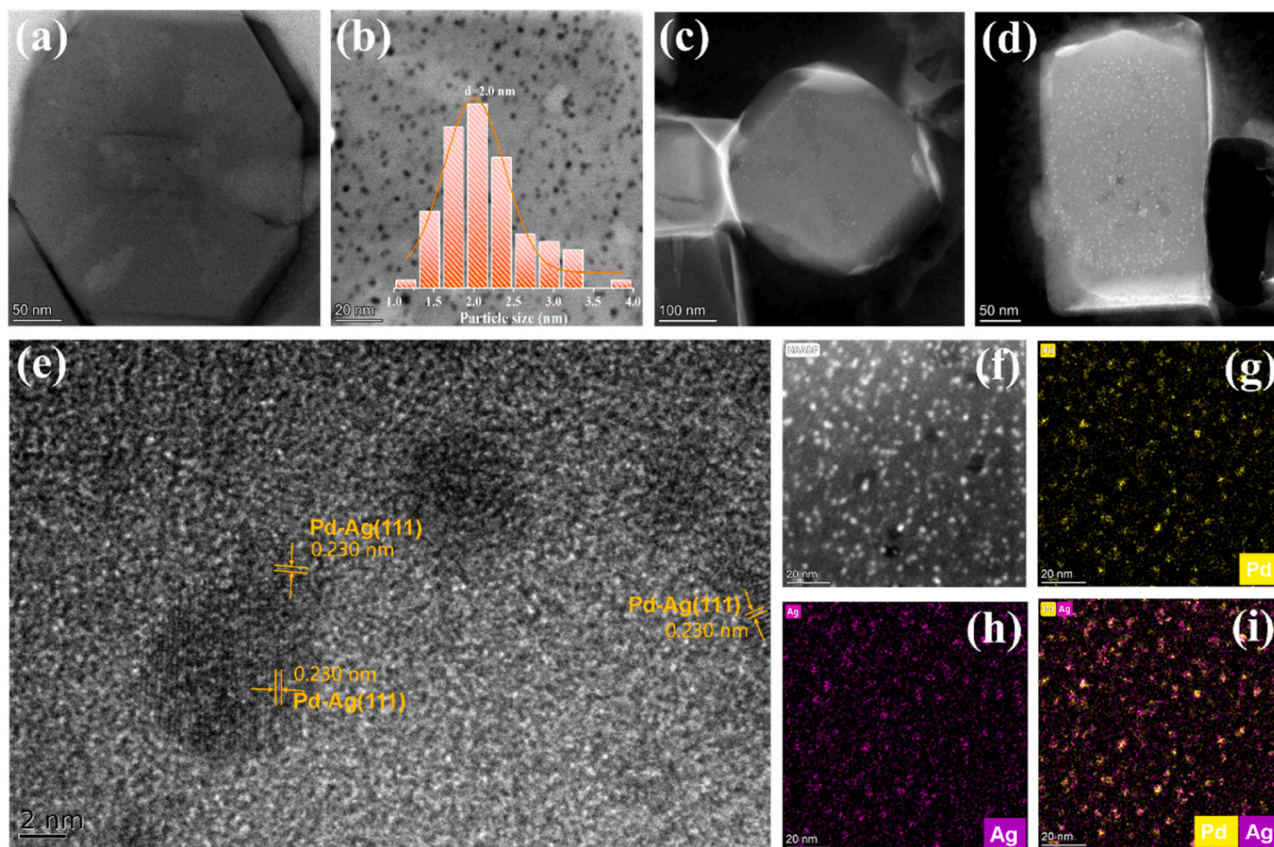


**Fig. 1.** (a-d, f) AC-HAADF-TEM (insert: metal cluster size distribution), (e) TEM image, (g-i) AC-EDX-Mapping images of the PdAg@S-1.



and 0.24 nm, respectively, while a lattice plane with a d spacing of 0.23 nm can be observed, which confirms the formation of the PdAg alloy phase [24]. The AC-EDX-mapping images (Fig. 1g-i) demonstrate that the Pd and Ag signals are maintained in the same position, revealing the homogeneous dispersion of Pd and Ag and the presence of the alloy structure [25]. The average particle size of the metals in the PdAg@S-1 (2.0 nm) catalyst was smaller than that of the supported PdAg/S-1 (4.0 nm), which was attributed to the confining effect of the rigid skeleton of the S-1 zeolite inhibiting the aggregation of the noble metals during the calcination or reduction process, resulting in smaller metal particle sizes and increased exposure of active sites. To further confirm that the PdAg in the PdAg@S-1 catalyst was effectively encapsulated, aberration-corrected high-angle annular dark-field TEM (AC-HAADF-TEM) was performed, and the results are shown in Fig. 1a-d, f. The smaller particle size of PdAg alloy encapsulated within the zeolite with uniform distribution is evident, implying that the encapsulation of PdAg particles inside the S-1 was successfully achieved.

The specific surface area and pore size information of the samples were explored by the  $N_2$ -adsorption desorption isotherm technique. The type I isotherms exhibited by all the samples in Fig. S6 indicate that the samples have a typical microporous structure, and the H3-type hysteresis loops in the relative pressure 0.9–1.0 can be traced back to mesopores stacked between the particles [26]. Details of the specific surface area and pore size of the samples are listed in Table S1. All the samples have a large specific surface area ( $450\text{--}465\text{ cm}^2\text{ g}^{-1}$ ), which is favorable for the dispersion of metals in the catalysts. Furthermore, the introduction of metals did not significantly change the specific surface area and pore structure of the carriers, implying that the metals encapsulated within the carriers are unlikely to obstruct the pores.

### 3.2. Chemical states and electronic properties of PdAg alloy structures

The surface electronic information of Pd and Ag in the reduced catalysts was measured using XPS technique, and the calibrated XPS spectra of Pd 3d and Ag 3d are shown in Fig. 2. The shielding effect of the zeolite shell caused the Pd 3d and Ag 3d signals in PdAg@S-1 to be invisible, further confirming that the Pd and Ag are dispersed inside the zeolite. Their locations lie beyond the detectable depth of the XPS technique, which is consistent with the TEM results. A similar situation was observed in the Pd@S-1 catalyst. A weak Ag 3d signal peak can be detected in Fig. 2b due to the easy migration and aggregation of metallic Ag to the zeolite surface. The spectra of Pd 3d<sub>5/2</sub> and Pd 3d<sub>3/2</sub> for the supported PdAg/S-1 catalyst was shown in Fig. 2a. The two peaks at 341.8 and 336.8 eV can be attributed to the Pd<sup>2+</sup> of the Pd 3d<sub>3/2</sub> and Pd 3d<sub>5/2</sub>, respectively, while the two peaks at 340.5 and 335.3 eV correspond to the metallic Pd [27]. The presence of Pd<sup>2+</sup> results from the surface oxidation of metallic Pd in the catalyst at room temperature. As

illustrated in Fig. 2b, the characteristic peaks at 368.4 and 374.5 eV in the Ag@S-1 sample are attributed to Ag<sup>0</sup> of Ag 3d<sub>5/2</sub> and Ag 3d<sub>3/2</sub>, respectively [28,29]. Notably, the Ag 3d spectrum of PdAg/S-1 is shifted to a lower binding energy compared to Ag@S-1 (negative shift of 0.5 eV compared to 368.4 eV for bulk silver), and the negative shift can be traced back to the electronic interactions between silver and palladium resulting in an electron transfer from Ag to Pd [30–33], the electron transfer direction is consistent with their electronegativities (EN) in Pauling scale, i.e., EN (Pd) = 2.20 eV, EN (Ag) = 1.93 eV, as well as work functions (WF), i.e., WF (Pd) = 5.2 eV, WF (Ag) = 4.26 eV [34]. The presence of an alloy phase has been confirmed in the HRTEM image of the PdAg@S-1 catalyst, so it is speculated that electron transfer was also present in PdAg@S-1, the charge density difference (CDD) during toluene degradation was calculated and the results are shown in Fig. S8. Represented by the yellow and blue regions are the accumulation and depletion of electrons. The large blue area around metallic Ag demonstrates the absence of electrons from Ag atoms.

XAFS measurements were applied to elucidate the microenvironmental information of Pd and Ag atoms in the samples. X-ray absorption near-edge structure (XANES) spectra of PdAg@S-1 and the corresponding reference samples are shown in Fig. 3a, b. In Fig. 3a, the normalized white line intensity of the Pd k-edge was located between PdO and Pd foil, suggesting that the Pd species carry positive charges. This phenomenon may be caused by the partial oxidation of Pd in air or the interaction with O in the zeolite skeleton [35]. The Ag k-edge white line intensity (Fig. 3b) is similar to that of the Ag foil, proving the presence of metallic Ag species. Fig. 3d, e show the Fourier transformed data of the k<sup>3</sup>-weighted extended X-ray absorption fine structure (FT-EXAFS) spectra of PdAg@S-1 and the reference sample. The FT-EXAFS curve and fitting results are shown in Fig. S9. The presence of metallic Pd is reconfirmed by the sharp peak at 2.5 Å in Fig. 3d, which corresponds to the Pd-Pd bond. The Pd-O peak at 1.6 Å indicates the absence of PdO species, which is consistent with the XPS results. The single intensity peak at 2.7 Å in the FT-EXAFS spectrum of Ag species is attributed to a continuous Ag-Ag bond (Fig. 3e) [36]. The wavelet transform (WT) was also performed for EXAFS analyses of PdAg@S-1 and the reference samples, the results are shown in Fig. 3c, f and Fig. S10. The WT EXAFS spectrum of PdAg@S-1 shows that the WT intensity maximum near 8.0 Å<sup>-1</sup> in k-space is resolved at 2.5 Å in R-space (Fig. 3c), which can be ascribed to Pd-Pd/Ag coordination. In addition, a maximum intensity of Ag-Ag coordination is shown at 4.5 Å<sup>-1</sup> in Fig. 3f, while intensity attributable to Ag-Ag/Pd coordination is also detected at 9.0 Å<sup>-1</sup>. Given the proximity of Pd and Ag in the periodic table, distinguishing between neighboring species around the central atom can be challenging. However, the radius of Ag atoms is slightly larger than that of Pd atoms, it is feasible to discern differences based on bond lengths. [37]. Comparing the metallic bonding distances

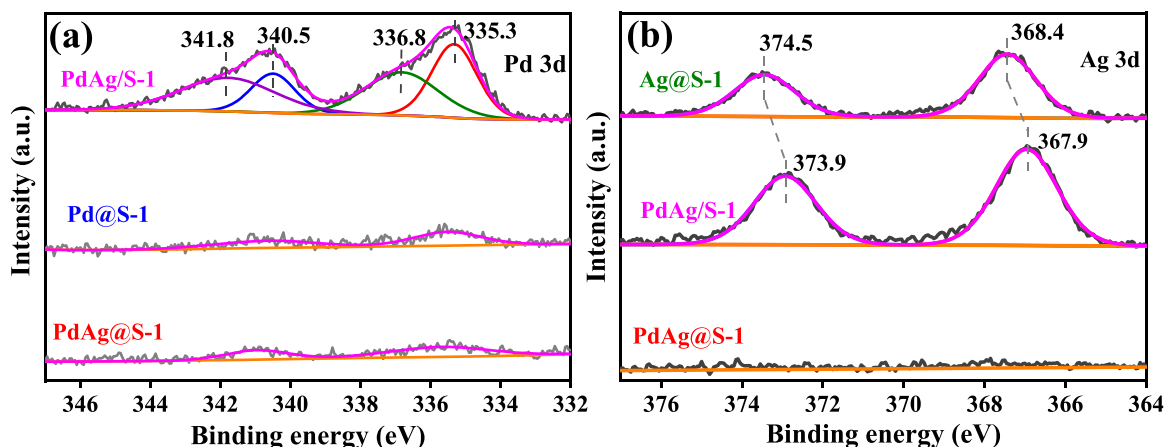


Fig. 2. XPS spectra of (a) Pd 3d and (b) Ag 3d of the PdAg@S-1 and related catalysts.

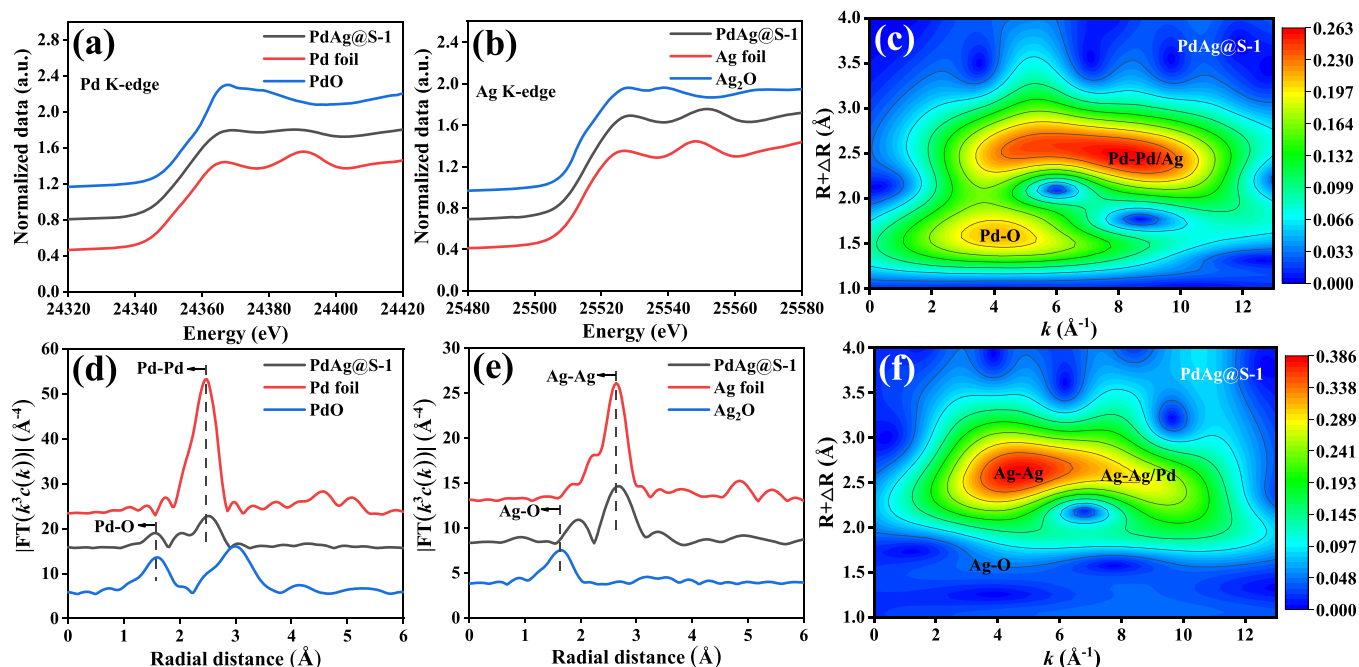


Fig. 3. (a) Pd k-edge and (b) Ag k-edge XANES, Fourier transform of  $k^3$ -weighted EXAFS spectra at the (d) Pd k-edge and (e) Ag k-edge, (c, f) wavelet transforms of PdAg@S-1 catalyst.

of the Pd and Ag foils in Table S2, respectively, an increase in the Pd-Pd/Ag bonding distances and a slight decrease in the Ag-Ag/Pd bonding distances in the PdAg@S-1 sample confirm the presence of Pd-Ag heteroatomic bonds [38,39].

### 3.3. Redox properties of catalysts

The reducibility of the samples was explored by using  $H_2$ -TPR, and the samples were not subjected to further reduction treatments before testing. The test results and hydrogen consumption are shown in Fig. 4a and Table S3, respectively. The TPR profiles of the samples containing elemental Pd all showed negative peaks before 100 °C related to the hydrogen desorption of  $PdH_x$  [40,41]. The reduction peaks displayed between 355 and 413 °C are attributed to the reduction of  $Ag^+$  [42–44]. The shielding effect of the zeolite shell layer causes the reduction peaks of Ag species to appear at higher temperatures. The reduction peaks of Pd and Ag were shifted to lower temperatures in the PdAg@S-1 and

PdAg/S-1 catalysts, which may be attributed to the electronic structure effect between the PdAg alloys that promotes the reducibility of the catalysts.

Next, the  $O_2$ -TPD technique was implemented to distinguish the type and mobility of oxygen species in various catalysts, and the results are shown in Fig. 4b. All samples presented two obvious oxygen desorption peaks, the  $O_\alpha$  in the low-temperature region (below 250 °C) represents desorption of oxygen physically adsorbed on surface of the catalyst, and the  $O_\beta$  in the high-temperature region (400–800 °C) is desorption of the lattice oxygen species inside the catalyst [45,46]. The oxygen consumption of PdAg@S-1 was significantly increased in the low-temperature region compared to the Pd@S-1 sample (Table S3), and the desorption peaks associated with lattice oxygen species shifted towards lower temperatures, suggesting that the catalyst possesses strong oxygen adsorption capability and high lattice oxygen mobility. However, the weaker oxygen adsorption capacity of the PdAg/S-1 sample could be attributed to the larger alloy particles formed on the external

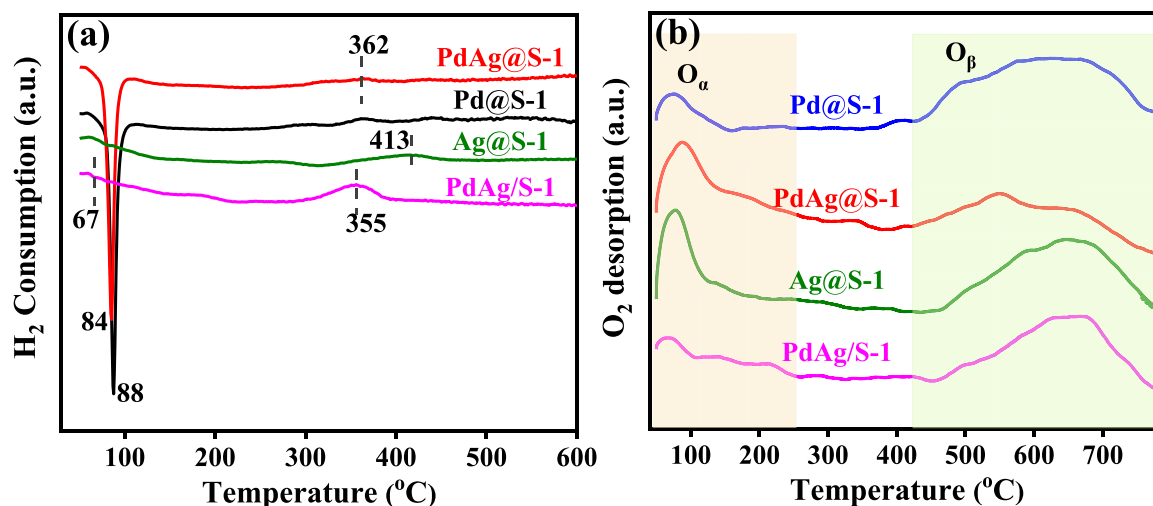


Fig. 4. (a)  $H_2$ -TPR, (b)  $O_2$ -TPD profiles of the PdAg@S-1 and related catalysts.

surface of the zeolite reducing the exposed active sites for adsorption of oxygen. Since the reaction was carried out below 300 °C, the adsorbed oxygen played an important role in the toluene degradation reaction.

### 3.4. Enhancement of toluene oxidation activity via PdAg alloy structure

The solid line in Fig. 5a illustrates toluene conversion as a function of reaction temperature for various catalysts. When the reaction gas containing 1000 ppm toluene was introduced into the catalyst, the Ag@S-1 catalyst exhibited limited activity for the total oxidation of toluene, achieving complete conversion at 270 °C. Generally, the noble metal Pd has a significant effect on the degradation of VOCs, which can also be reflected in the catalytic performance of the Pd@S-1 sample for toluene. Surprisingly, after constructing the PdAg alloy structure inside the zeolite, the PdAg@S-1 catalyst completely converted toluene to harmless products at temperatures as low as 180 °C (Fig. 5a and Fig. S11), which was significantly better than the catalytic performance of Pd@S-1 and Ag@S-1 catalysts. To compare the catalytic performances of all catalysts more clearly, the specific activity data of the samples and the actual metal contents obtained by the ICP technique are listed in Table S4. However, the supported PdAg/S-1 catalyst ( $T_{90}=256$  °C) exhibited significantly lower catalytic activity towards toluene compared to the PdAg@S-1 catalyst, which was attributed to higher dispersion of metal in the zeolite of PdAg@S-1, and the smaller alloy particle size could expose more active sites. The catalytic activity of Pd-based catalysts for toluene from previous literature is documented in Table S5. The comparison demonstrates the advantages of PdAg@S-1 in toluene degradation. In addition, the alloy structure inside the zeolite also affected the adsorption capacity of the catalyst for toluene (Fig. S12). The time required for toluene adsorption to reach saturation on PdAg@S-1 was the longest, indicating that PdAg@S-1 possesses the highest toluene adsorption capability. For the PdAg/S-1 catalyst, the adsorption capacity was higher in the initial stage, but gradually decreased as time increased, which could be attributed to the larger metal clusters on the outer surface of the catalyst hindering the diffusion of toluene.

Subsequently, 5 vol% H<sub>2</sub>O was introduced into the reaction gas to test the humidity resistance of the various catalysts, with the results depicted as dashed lines in Fig. 5a. The impact of water vapor on Ag@S-1 was more pronounced below 240 °C, whereas its activity converged with that observed under dry conditions as the temperature rose. Interestingly, the negative effect of water molecules on the encapsulated catalysts is much less than that on the supported catalysts due to the shielding effect of hydrophobic zeolite shell on the water vapor preventing its adsorption on the internal active sites [47,48]. The electronic structure interaction between the alloys further mitigates the impact of

water molecules on Pd, ensuring that the activity of PdAg@S-1 in a humid environment remains superior to that of Pd@S-1. The above results demonstrated that the strategy of constructing PdAg alloys inside the zeolite improved the water resistance of the catalyst. Kinetic experiments of the catalysts were carried out excluding the effect of mass and heat transfer (Table S6-S8). The Arrhenius plots and apparent activation energy data for the various catalysts are shown in Fig. 5b and Table S9. The apparent activation energies ( $E_a$ ) of the samples were in the following order: Ag@S-1 (112.8 kJ·mol<sup>-1</sup>) > PdAg/S-1 (98.4 kJ·mol<sup>-1</sup>) > Pd@S-1 (82.0 kJ·mol<sup>-1</sup>) > PdAg@S-1 (76.9 kJ·mol<sup>-1</sup>), which was consistent with their toluene catalytic performance. In addition, the TOF values of the three Pd-based catalysts were calculated and the results are displayed in Table S9. The highest TOF value was observed in the PdAg@S-1 catalyst (10.15×10<sup>-2</sup> s<sup>-1</sup> at 170 °C), which was approximately twice that of the PdAg/S-1 sample.

### 3.5. Stability evaluation

Catalysts are often reused to ensure economic benefits, so cycling stability is a crucial factor in evaluating the performance of catalysts. Fig. 6a demonstrates the results of five cycling tests for the PdAg@S-1 sample, with the experimental conditions remaining consistent for each test. The catalytic activity of PdAg@S-1 catalyst remained almost unchanged after five cycle tests, and it can be inferred that there was no phase separation of the PdAg alloy during the reaction process. This inference stems from the fact that degradation activities of Pd@S-1, Ag@S-1, and PdAg@S-1 for toluene are very different, and catalytic activity of PdAg@S-1 catalyst would be changed if alloying phases in the catalyst were separated. The results of five cycle tests also confirmed excellent cycling stability of PdAg@S-1 catalyst.

Next, long-term stability tests were conducted on the PdAg@S-1 and PdAg/S-1 samples, with the results presented in Fig. 6b. The degradation efficiency of the PdAg@S-1 samples remained unchanged after 100 h of toluene oxidation experiments at a temperature of 177 °C (the conversion of toluene was 75%). Both XRD patterns and TEM images (Fig. S13 and S14) demonstrate that the catalyst after stability testing exhibits high crystallinity and an intact morphological structure, suggesting that PdAg@S-1 has outstanding stability. However, to maintain the same toluene conversion, a long-term stability experiment was conducted at 250 °C for the PdAg/S-1 sample. Notably, the activity of PdAg/S-1 continued to decrease during the test period (75% conversion dropped to 40%). Raman results of the reacted catalyst revealed the accumulation of carbon deposits on PdAg/S-1 after the long term stability experiments, which was considered to be one of the reasons for catalyst deactivation (Fig. S15). Aggregation of the active components exposed to the outer surface of the zeolite during the prolonged testing may be

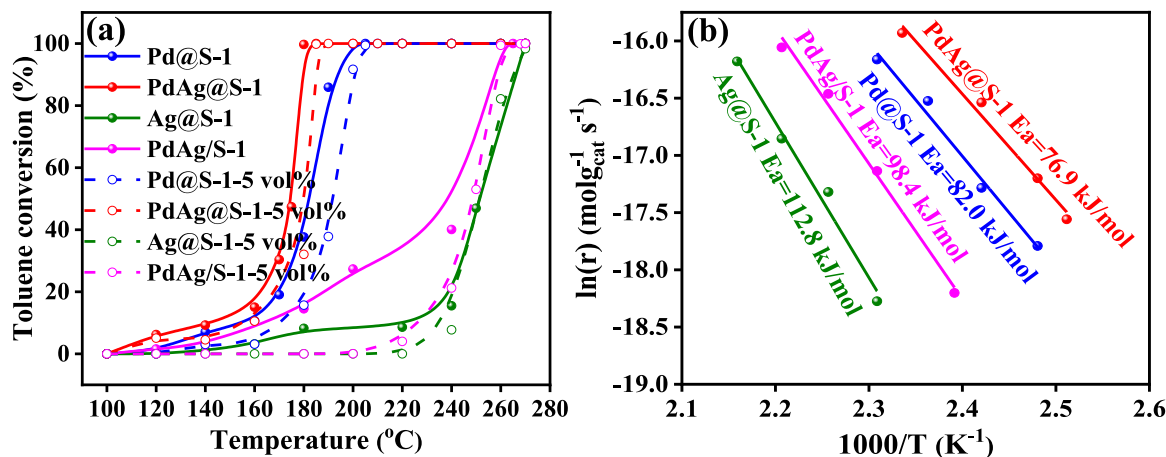
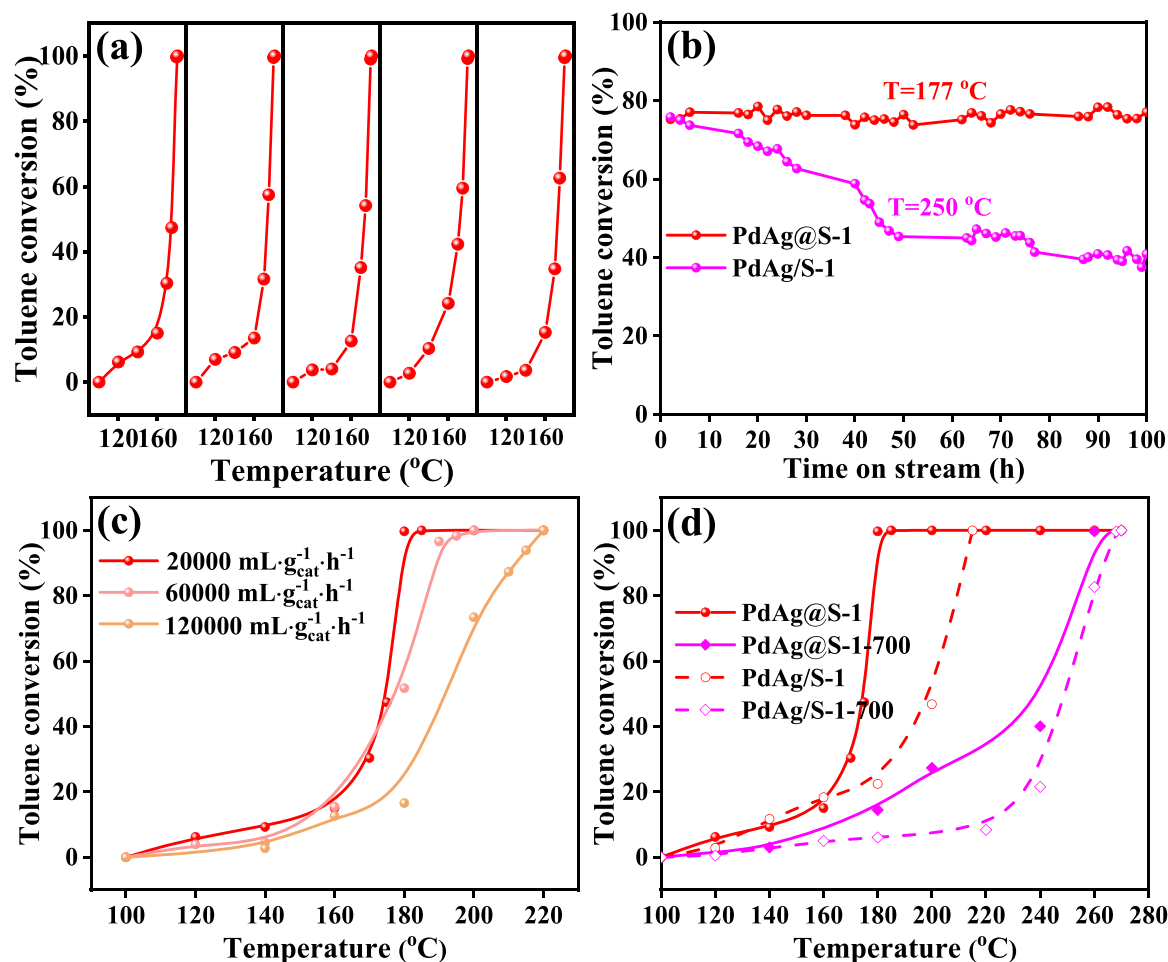


Fig. 5. (a) Plots of toluene conversion in dry (solid line) and humid (dashed line) atmospheres, (b) Arrhenius plots of the various catalysts. Conditions: (a) 0.1% C<sub>7</sub>H<sub>8</sub> + Air (solid line) and 0.1% C<sub>7</sub>H<sub>8</sub> + 5 vol% H<sub>2</sub>O + Air (dashed line), (b) 0.1% C<sub>7</sub>H<sub>8</sub> + Air. WHSV: (a) 20000 mL·g<sub>cat</sub><sup>-1</sup>·h<sup>-1</sup>, (b) 100000 mL·g<sub>cat</sub><sup>-1</sup>·h<sup>-1</sup>.



**Fig. 6.** (a) Cycling performance of the PdAg@S-1, (b) long-term stability performance, (c) the influence of WHSV on the PdAg@S-1, (d) high-temperature resistance test. Conditions: (a-d) 0.1% C<sub>7</sub>H<sub>8</sub> + Air. WHSV: (a, b, d) 20000 mL·g<sub>cat</sub><sup>-1</sup>·h<sup>-1</sup>.

another factor for the decrease in activity. Fig. 6c reveals the catalytic oxidation performance of PdAg@S-1 for toluene at different weight hourly space velocity (WHSV). The degradation efficiency of PdAg@S-1 for toluene showed a minor decline as the WHSV increased to 60,000 mL·g<sub>cat</sub><sup>-1</sup>·h<sup>-1</sup>. when the WHSV was increased to 120,000 mL·g<sub>cat</sub><sup>-1</sup>·h<sup>-1</sup>, the PdAg@S-1 catalyst was still able to realize the complete degradation of toluene at 220 °C, indicating that the PdAg@S-1 could still maintain a good catalytic performance at high WHSV.

High-temperature resistance is another important index to measure the practical applicability of catalysts. In this regard, PdAg@S-1 and PdAg/S-1 were roasted at 700 °C for 2 h in the N<sub>2</sub> atmosphere. The catalysts after roasting were noted as PdAg@S-1-700 and PdAg/S-1-700, respectively, and their catalytic properties are shown in Fig. 6d. The degradation performance of the catalysts for toluene decreased after high-temperature treatment, but the encapsulated PdAg@S-1-700 showed superior catalytic activity compared with the supported PdAg/S-1-700, and it could still degrade toluene completely before 215 °C. The XRD spectra of PdAg@S-1-700 and PdAg/S-1-700 are shown in Fig. S16. The high-temperature treatment did not destroy the structure of the two catalysts, and the diffraction peaks associated with the Pd and Ag species were not detected, indicating that the two metals are still highly dispersed. The TEM images in Fig. S17 also confirm that PdAg@S-1-700 and PdAg/S-1-700 have intact structures. Notably, the average metal particle size in PdAg/S-1-700 increased significantly compared to that before the high-temperature treatment, it is still below the detection limit of XRD. In contrast, the average metal particle size in PdAg@S-1-700 increased slightly, which is attributed to i) the encapsulation

strategy that allows the metal to be well anchored by the zeolite shell layer and pores, ii) the formation of PdAg alloying components inhibited the migratory aggregation of the same metal element under high-temperature conditions. In conclusion, the zeolite encapsulated PdAg alloy catalyst has excellent stability and meets certain industrial needs.

### 3.6. Insights into reactant degradation on alloy structures

To further investigate the adsorption properties of the catalyst surface on reactant molecules, the adsorption energy of toluene and oxygen molecules were calculated by employing density functional theory (DFT), and the results are shown in Fig. 7a. The (200) crystal plane of S-1 and the atomic ratio of Pd, Ag were determined based on the XRD spectrum and the actual content measured by ICP, respectively. The optimized top and side view structures of Pd<sub>3</sub>Ag<sub>1</sub>@S-1(200) are displayed in Fig. S18. In Fig. 7a, toluene molecules chemisorbed on the catalyst surface with an adsorption energy of 1.040 eV. The projected density of states (PDOS) results indicate that during toluene adsorption, hybridization occurs between the electron clouds of C<sup>⊙</sup> (C attached to the methyl group) and C<sup>⊙</sup> (C adjacent to C<sup>⊙</sup>), and then C 2p orbitals hybridize with the 3d orbitals of Pd, resulting in the formation of the C-Pd bonds with the bond lengths of 2.204 and 2.306 Å, respectively. When toluene and oxygen molecules are co-adsorbed by the active sites on the catalyst surface, the toluene molecules are preferentially adsorbed by the electron-rich Pd, and the bond lengths of C<sup>⊙</sup> and C<sup>⊙</sup> hybridized with the Pd atoms are 2.151 and 2.285 Å, respectively, which are shorter than that of the C-Pd bond formed by the singly adsorbed



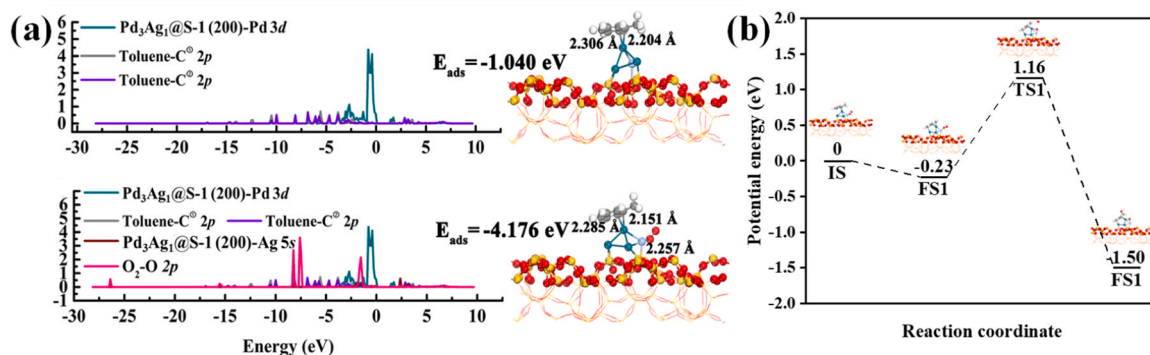


Fig. 7. Configurations and PDOS of (a) toluene adsorption, toluene and O<sub>2</sub> co-adsorption on the Pd<sub>3</sub>Ag<sub>1</sub>@S-1 (200) structure, (b) removal paths and energy barriers of toluene on the Pd<sub>3</sub>Ag<sub>1</sub>@S-1 (200).

toluene molecules, suggesting that the C-Pd bond formed in the case of co-adsorption is more stable. The oxygen molecule is adsorbed at the electron-deficient Ag site, giving an Ag-O bond with a bond length of 2.257 Å. The active site shows stronger adsorption when both toluene and oxygen molecules are adsorbed, with an adsorption energy of 4.176 eV. The electronic interaction between Pd and Ag promotes the activation of oxygen and the dissociation of C-H bonds on the alloy structure, thus facilitating the deep oxidation of toluene.

Fig. 7b illustrates the degradation of toluene to another transient intermediate benzyl alcohol on the catalyst surface. The degradation process of toluene on the catalyst surface can be categorized into the

following three steps: (1)  $\text{C}_6\text{H}_5\text{CH}_3_{\text{ads}} + \text{O}_{2\text{ads}} \rightarrow \text{C}_6\text{H}_5\text{CH}_2\text{-Pd} + \text{Ag-O-OH}$ , (2)  $\text{C}_6\text{H}_5\text{CH}_2\text{-Pd} + \text{Ag-O-OH} \rightarrow \text{C}_6\text{H}_5\text{CH}_2 + \text{Pd-O-Ag} + \text{OH}^*$ , (3)  $\text{C}_6\text{H}_5\text{CH}_2 + \text{OH}^* \rightarrow \text{C}_6\text{H}_5\text{CH}_2\text{OH}$ . Toluene and oxygen molecules are co-adsorbed on the active site on the catalyst surface, and the optimized structure is noted as 0 eV. In the first step, the C-H bond on the methyl group is dissociated, and the dissociated H atoms bind to the gas-phase oxygen molecules, and this step is accompanied by a little energy (0.23 eV). In the second step, the O-O bond in the O<sub>2</sub> molecule is broken, and the broken O atoms are bonded with H atoms and PdAg alloys to synthesize OH\* radicals and Pd-O-Ag structures, respectively. This step is realized by breaking through a high energy barrier (1.16 eV).

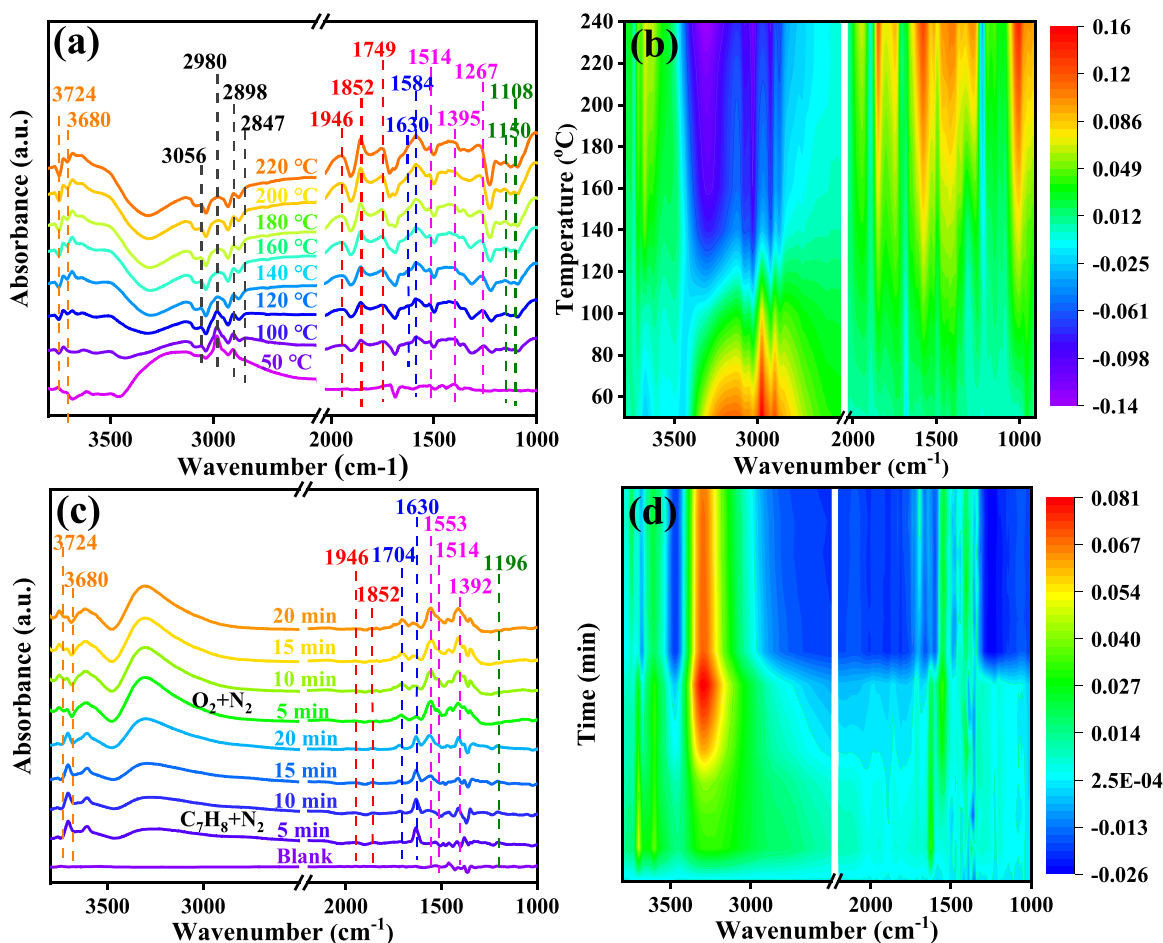


Fig. 8. In situ DRIFT spectra of toluene oxidation over PdAg@S-1 catalyst at (a, b) 50–220 °C and (c, d) 180 °C, respectively. Condition: (a, b) 0.1% C<sub>7</sub>H<sub>8</sub> + 20% O<sub>2</sub> + 79.9% N<sub>2</sub> and flow rate = 30 mL·min<sup>-1</sup>, (c, d) adsorption with 0.1% C<sub>7</sub>H<sub>8</sub> + 99.9% N<sub>2</sub> for 30 min, then switched to 20% O<sub>2</sub> + 80% N<sub>2</sub> adsorption for 30 min, flow rate = 30 mL·min<sup>-1</sup>.



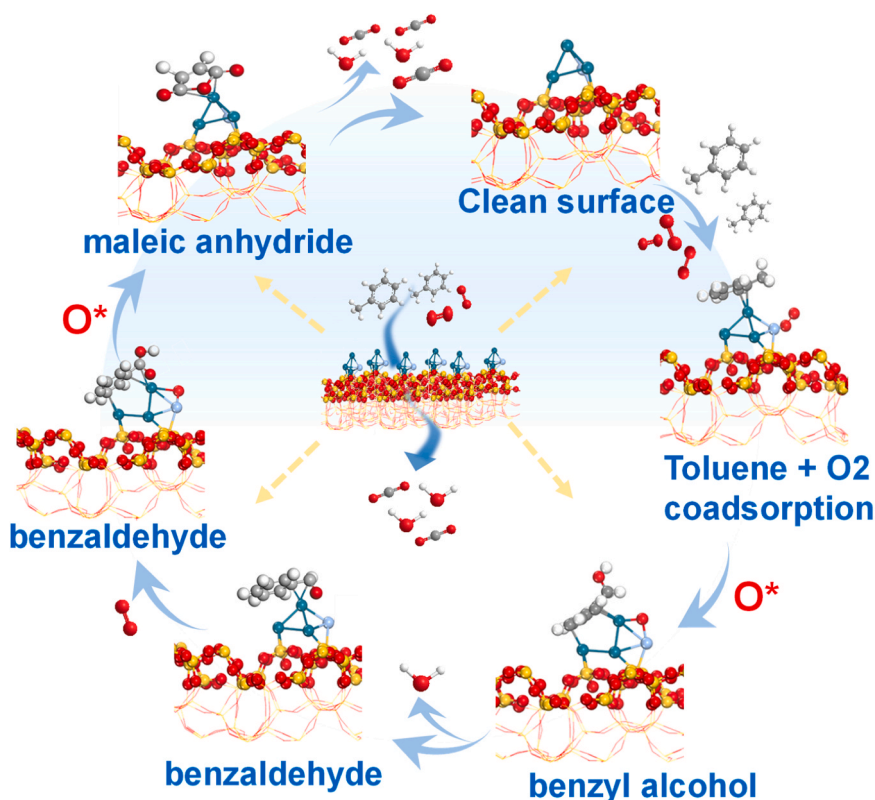
Subsequently, in the third step, the free  $\text{OH}^*$  interacts with  $\text{C}_6\text{H}_5\text{CH}_2$  adsorbed on the palladium site to give alcohols, a process accompanied by the release of energy. The Pd-O-Ag structure continues to play an active role in the subsequent deep oxidation. This calculation is in agreement with the in situ DRIFTS results, where gas-phase oxygen molecules play an important role in these processes.

### 3.7. Mechanism of toluene degradation over PdAg@S-1

The in situ DRIFTS technique was utilized to further investigate the generation of intermediates and to provide insight into the mechanism of the catalytic oxidation of toluene over the PdAg@S-1 catalyst. Firstly, the toluene adsorption experiment was carried out at  $50^\circ\text{C}$  for different times, and the results are shown in Fig. S19. The vibrational peaks in the range of  $2840\text{--}3060\text{ cm}^{-1}$  are caused by the stretching vibration of C-H on the benzene ring, and the bands at  $1614, 1490\text{ cm}^{-1}$  are attributed to the in-plane skeletal vibrations of the benzene ring structure [49,50]. The characteristic band associated with toluene starts to appear at the initial stage of adsorption and rises rapidly within a short time, reaching adsorption saturation at about 22 min. It indicates that the PdAg@S-1 catalyst has strong adsorption of toluene, which provides favorable conditions for the subsequent catalytic oxidation reaction. Subsequently, toluene oxidation experiments were carried out under the presence of gas-phase oxygen, the temperature interval was chosen to be  $50\text{--}220^\circ\text{C}$  (Fig. 8a, b). The band at  $3724\text{ cm}^{-1}$  was assigned to the internally isolated Si-OH, and the band at  $3680\text{ cm}^{-1}$  was assigned to the hydrogen-bonded Si-OH partially confined in the micropores and shallow cavities on the outer surface [51,52], respectively. As the temperature increased, toluene was gradually desorbed and the vibrational peaks in the range of  $2840\text{--}3060\text{ cm}^{-1}$  showed a decreasing trend. In addition, the characteristic peaks of a series of intermediates gradually appeared. The bands at  $1946, 1852, 1749\text{ cm}^{-1}$  are attributed to asymmetric and symmetric  $\text{C}=\text{O}$  stretching vibration of maleic anhydride [12,53,54]. The bands at  $1630$  and  $1584\text{ cm}^{-1}$  can be regarded as

$\text{C}=\text{O}$  stretching vibrations of benzaldehyde species [55]. The band at  $1514, 1395$ , and  $1267\text{ cm}^{-1}$  corresponds to the  $\text{COO}^-$  asymmetry and symmetry vibration of benzoate species [56–58]. The bands at  $1150$  and  $1108\text{ cm}^{-1}$  belong to the C-O stretching of vibrational of alkoxide species [59,60]. The peaks of the intermediates all rise gradually during the increase in temperature, indicating that toluene undergoes intense oxidation.

The in situ DRIFTS of toluene oxidized over PdAg@S-1 catalyst in the absence of gas-phase oxygen are shown in Fig. 8c, d. The characteristic bands attributed to some intermediates can still be detected, however, the intensity of the characteristic peaks of the intermediate species hardly changed with the increase of oxidation time, indicating that the deep oxidation of toluene under conditions without gas-phase oxygen participation was inefficient. Notably, when gas-phase oxygen species were introduced into the system, the characteristic peaks of benzyl alcohol ( $1196\text{ cm}^{-1}$ ) and benzaldehyde ( $1630\text{ cm}^{-1}$ ) species rapidly weakened or even disappeared, and the bands of benzoic acid species ( $1395\text{--}1553\text{ cm}^{-1}$ ) were significantly enhanced, suggesting that accumulation of benzoic acid species occurs and that ring-opening of benzoic acid is the rate-determining step. The gradual undetectable phenomenon of the anhydride species ( $1852, 1946\text{ cm}^{-1}$ ) suggests that toluene has been completely oxidized to  $\text{H}_2\text{O}$  and  $\text{CO}_2$ . This is confirmed by the trend of significant enhancement of broad peaks in the  $3000\text{--}3500\text{ cm}^{-1}$  range attributed to the hydroxyl group of the  $\text{H}_2\text{O}$  molecule. Gas-phase oxygen molecules play an important role in the oxidation reaction of toluene. The oxidation reaction of toluene mainly follows the Langmuir-Hinshelwood (L-H) mechanism and the degradation pathway of toluene is shown in Scheme 1. Due to the strong adsorption of toluene by the zeolite, toluene was adsorbed abundantly on the active sites of the PdAg@S-1 surface. Gas-phase oxygen molecules were activated to reactive oxygen species at the PdAg alloy sites, and the adsorbed toluene was oxidized to benzene ring intermediates by the reactive oxygen and finally mineralized to non-toxic and harmless  $\text{H}_2\text{O}$  and  $\text{CO}_2$ . Toluene is mineralized by the following pathway: toluene→benzyl



Scheme 1. Toluene degradation mechanism over the PdAg@S-1 catalyst.

alcohol→benzaldehyde→benzoate→maleic anhydride→CO<sub>2</sub> and H<sub>2</sub>O. The reactive oxygen species at the alloying sites significantly contributed to the ring opening and deep oxidation of toluene.

#### 4. Conclusions

In summary, a zeolite-encapsulated PdAg alloy catalyst (PdAg@S-1) was prepared and applied to the degradation of toluene. The PdAg@S-1 exhibits high toluene degradation performance ( $T_{90}$  = 179 °C), and this catalytic activity was maintained under humid conditions. The encapsulation strategy and alloy structure effectively anchored the noble metals, providing the catalyst with outstanding stability and resistance. The results of XAFS and DFT calculations indicate that the formation of the alloy phase altered the chemical environment of the active species, promoting adsorption towards toluene and oxygen molecules. The in situ DRIFTS results reveal that the oxidation of toluene over the PdAg@S-1 catalyst follows the L-H mechanism, with gas-phase oxygen continuously being activated into active oxygen, participating in the entire redox reaction. This work provides a new strategy for the development of high-performance noble metal-based catalysts and the effective elimination of VOCs.

#### CRediT authorship contribution statement

**Tianyao He:** Data curation, Formal analysis. **Wenming Liu:** Methodology, Supervision, Writing – review & editing. **Hongxiang Zhang:** Software, Validation. **Yunbo Yu:** Methodology, Supervision. **Qiuli Zhang:** Conceptualization, Data curation, Investigation, Writing – original draft. **Gan Li:** Conceptualization, Data curation, Writing – original draft. **Guobo Li:** Software, Validation. **Honggen Peng:** Funding acquisition, Project administration, Supervision, Writing – review & editing.

#### Declaration of Competing Interest

The authors declare that they have no known competing financial interests or personal relationships that could have appeared to influence the work reported in this paper.

#### Data availability

Data will be made available on request.

#### Acknowledgments

This work was supported by the National Natural Science Foundation of China (21976078, 22276086, 22306086), the Natural Science Foundation of Jiangxi Province (2020ACB213001, 20232BAB213029, 20232BAB213028), and the Natural Science Foundation of Chongqing (CSTB2023NSCQ-MSX0950), all of which are greatly acknowledged by the authors.

#### Appendix A. Supporting information

Supplementary data associated with this article can be found in the online version at [doi:10.1016/j.apcatb.2024.124051](https://doi.org/10.1016/j.apcatb.2024.124051).

#### References

- X. Li, L. Zhang, Z. Yang, P. Wang, Y. Yan, J. Ran, Adsorption materials for volatile organic compounds (VOCs) and the key factors for VOCs adsorption process: a review, *Sep. Purif. Technol.* 235 (2020) 116213.
- Ç. Güngör, M. Şakir Ece, Competitive adsorption of VOCs (benzene, xylene and ethylbenzene) with Fe<sub>3</sub>O<sub>4</sub>@SiO<sub>2</sub>-NH@BENZOPHENONE magnetic nano-adsorbents, *Chem. Eng. J.* 475 (2023) 146034.
- Y. Sun, Y. Liu, G. Yue, J. Cao, C. Li, J. Ma, Vapor-phase biodegradation and natural attenuation of petroleum VOCs in the unsaturated zone: a microcosm study, *Chemosphere* 336 (2023) 139275.
- B. Wang, Q. Yang, B. Li, H. Ma, Y. Xuan, C. Gao, Y. Liang, K. Zhang, Q. Chang, O. Broesicke, H. Wang, D. Wang, T. Luan, K. Han, C. Lu, J. Crittenden, Heterostructure-strengthened metal-support interaction of single-atom Pd catalysts enabling efficient oxygen activation for CO and VOC oxidation, *Appl. Catal. B-Environ.* 332 (2023) 122753.
- Y. Ren, X. Lei, H. Wang, J. Xiao, Z. Qu, Enhanced catalytic performance of La-Doped CoMn<sub>2</sub>O<sub>4</sub> catalysts by regulating oxygen species activity for VOCs oxidation, *ACS Catal.* 13 (2023) 8293–8306.
- Y. Shen, J. Deng, X. Hu, X. Chen, H. Yang, D. Cheng, D. Zhang, Expediting toluene combustion by harmonizing the Ce–O strength over Co-doped CeZr oxide catalysts, *Environ. Sci. Technol.* 57 (2023) 1797–1806.
- K. Zhang, H. Ding, W. Pan, X. Mu, K. Qiu, J. Ma, Y. Zhao, J. Song, Z. Zhang, Research progress of a composite metal oxide catalyst for VOC degradation, *Environ. Sci. Technol.* 56 (2022) 9220–9236.
- L. Zhang, L. Xue, B. Lin, Q. Zhao, S. Wan, Y. Wang, H. Jia, H. Xiong, Noble metal single-atom catalysts for the catalytic oxidation of volatile organic compounds, *ChemSusChem* 15 (2022) 202102494.
- G. Vilé, D. Albani, M. Nachtegaal, Z. Chen, D. Dontsova, M. Antonietti, N. López, J. Pérez-Ramírez, A stable single-site palladium catalyst for hydrogenations, *Angew. Chem. Int. Ed.* 54 (2015) 11265–11269.
- M. Guo, H. Li, Y. Ren, X. Ren, Q. Yang, C. Li, Improving catalytic hydrogenation performance of Pd nanoparticles by electronic modulation using phosphine ligands, *ACS Catal.* 8 (2018) 6476–6485.
- Y.-H. Chin, C. Buda, M. Neurock, E. Iglesia, Consequences of metal–oxide interconversion for C–H bond activation during CH<sub>4</sub> reactions on Pd catalysts, *J. Am. Chem. Soc.* 135 (2013) 15425–15442.
- F. Bi, Z. Zhao, Y. Yang, W. Gao, N. Liu, Y. Huang, X. Zhang, Chlorine-coordinated Pd single atom enhanced the chlorine resistance for volatile organic compound degradation: mechanism study, *Environ. Sci. Technol.* 56 (2022) 17321–17330.
- Y. Ma, X. Tang, J. Hu, Y. Ma, W. Chen, Z. Liu, S. Han, C. Xu, Q. Wu, A. Zheng, L. Zhu, X. Meng, F.-S. Xiao, Design of a small organic template for the synthesis of self-pillared pentasil zeolite nanosheets, *J. Am. Chem. Soc.* 144 (2022) 6270–6277.
- S. Mo, J. Li, R. Liao, P. Peng, J. Li, J. Wu, M. Fu, L. Liao, T. Shen, Q. Xie, D. Ye, Unraveling the decisive role of surface CeO<sub>2</sub> nanoparticles in the Pt–CeO<sub>2</sub>/MnO<sub>2</sub> hetero-catalysts for boosting toluene oxidation: synergistic effect of surface decorated and intrinsic O-vacancies, *Chem. Eng. J.* 418 (2021) 129399.
- G. Ercolino, P. Stelmachowski, G. Gryzbek, A. Kotarba, S. Specchia, Optimization of Pd catalysts supported on Co<sub>3</sub>O<sub>4</sub> for low-temperature lean combustion of residual methane, *Appl. Catal. B-Environ.* 206 (2017) 712–725.
- J. Lee, E.J. Jang, D.G. Oh, J. Szanyi, J.H. Kwak, Morphology and size of Pt on Al<sub>2</sub>O<sub>3</sub>: the role of specific metal-support interactions between Pt and Al<sub>2</sub>O<sub>3</sub>, *J. Catal.* 385 (2020) 204–212.
- Y. Shi, Z. Li, J. Wang, R. Zhou, Synergistic effect of Pt/Ce and USY zeolite in Pt-based catalysts with high activity for VOCs degradation, *Appl. Catal. B-Environ.* 286 (2021) 119936.
- J. Liu, Y. Wang, Z. Dai, C.Q. Jia, L. Yang, J. Liu, Y. Chen, L. Yao, B. Wang, W. Huang, W. Jiang, Recent advances in Zeolite-Based catalysts for volatile organic compounds decontamination by thermal catalytic oxidation, *Sep. Purif. Technol.* 330 (2024) 125339.
- W. Yuan, D. Zhang, Y. Ou, K. Fang, B. Zhu, H. Yang, T.W. Hansen, J.B. Wagner, Z. Zhang, Y. Gao, Y. Wang, Direct in situ TEM visualization and insight into the facet-dependent sintering behaviors of gold on TiO<sub>2</sub>, *Angew. Chem. Int. Ed.* 57 (2018) 16827–16831.
- G. Prieto, J. Zečević, H. Friedrich, K.P. de Jong, P.E. de Jongh, Towards stable catalysts by controlling collective properties of supported metal nanoparticles, *Nat. Mater.* 12 (2012) 34–39.
- S. Xie, J. Deng, Y. Liu, Z. Zhang, H. Yang, Y. Jiang, H. Arandiyani, H. Dai, C.T. Au, Excellent catalytic performance, thermal stability, and water resistance of 3DOM Mn<sub>2</sub>O<sub>3</sub>-supported Au–Pd alloy nanoparticles for the complete oxidation of toluene, *Appl. Catal., A* 507 (2015) 82–90.
- Q. Liu, M. Wen, Y. Guo, S. Song, G. Li, T. An, Efficient catalytic combustion of cyclohexane over PdAg/Fe<sub>2</sub>O<sub>3</sub> catalysts under low-temperature conditions: establishing the degradation mechanism using PTR-TOF-MS and in Situ DRIFTS, *ACS Appl. Mater. Interfaces* 14 (2022) 55503–55516.
- S. Song, Q. Liu, J. Xiong, M. Wen, T. An, Promotional effects of Ag on catalytic combustion of cyclohexane over PdAg/Ti-SBA-15, *J. Catal.* 421 (2023) 77–87.
- H. Liu, M. Wang, X. Zhang, J. Ma, G. Lu, High efficient photocatalytic hydrogen evolution from formaldehyde over sensitized Ag@Ag-Pd alloy catalyst under visible light irradiation, *Appl. Catal. B-Environ.* 237 (2018) 563–573.
- R. Li, W. Yao, Y. Jin, W. Jia, X. Chen, J. Chen, J. Zheng, Y. Hu, D. Han, J. Zhao, Selective hydrogenation of the C=C bond in cinnamaldehyde over an ultra-small Pd-Ag alloy catalyst, *Chem. Eng. J.* 351 (2018) 995–1005.
- L. Zhang, X. Wang, Y. Chen, Rapid synthesis of uniform nano-sized silicalite-1 zeolite crystals under atmospheric pressure without wastes discharge, *Chem. Eng. J.* 382 (2020) 122913.
- K. Yang, R. Wang, D. Xu, X. Ma, D. Ding, M. Zhang, L. Zhang, Z. Bai, Z. Zhu, H. Lü, Metal-acid dual sites in Pd/SiO<sub>2</sub>-Al<sub>2</sub>O<sub>3</sub> synergistically catalyze selective hydrogenation-etherification of furfural to bioether, *J. Catal.* 425 (2023) 170–180.
- B. Mishra, D. Ghosh, B.P. Tripathi, Finely dispersed AgPd bimetallic nanoparticles on a polydopamine modified metal organic framework for diverse catalytic applications, *J. Catal.* 411 (2022) 1–14.
- A.V. Rassolov, I.S. Mashkovsky, G.N. Baeva, G.O. Bragina, N.S. Smirnova, P. V. Markov, A.V. Bukhtiyarov, J. Wärmä, A.Y. Stakheev, D.Y. Murzin, Liquid-phase hydrogenation of 1-Phenyl-1-propyne on the Pd<sub>1</sub>Ag<sub>3</sub>/Al<sub>2</sub>O<sub>3</sub> single-atom alloy catalyst: kinetic modeling and the reaction mechanism, *Nanomater* 11 (2021) 3286.

- [30] R. Chanerika, M.L. Shoji, M. Prato, H.B. Friedrich, The effect of coating Pd/Al<sub>2</sub>O<sub>3</sub> and PdAg/Al<sub>2</sub>O<sub>3</sub> catalysts with [BMIM][DCA] for the selective hydrogenation of 1-Octyne in 1-Octene, *ChemCatChem* 15 (2022) 202201043.
- [31] R. Lamb, Surface characterisation of Pd-Ag/Al<sub>2</sub>O<sub>3</sub> catalysts for acetylene hydrogenation using an improved XPS procedure, *Appl. Catal.*, A. 268 (2004) 43–50.
- [32] J.A. Zamora Zeledón, M.B. Stevens, G.T.K.K. Gunasooriya, A. Gallo, A.T. Landers, M.E. Kreider, C. Hahn, J.K. Nørskov, T.F. Jaramillo, Tuning the electronic structure of Ag-Pd alloys to enhance performance for alkaline oxygen reduction, *Nat. Commun.* 12 (2021) 620.
- [33] K. Tedsree, T. Li, S. Jones, C.W.A. Chan, K.M.K. Yu, P.A.J. Bagot, E.A. Marquis, G. D.W. Smith, S.C.E. Tsang, Hydrogen production from formic acid decomposition at room temperature using a Ag–Pd core–shell nanocatalyst, *Nat. Nanotechnol.* 6 (2011) 302–307.
- [34] X.L. Xing, Y.F. Zhao, H. Li, C.T. Wang, Q.X. Li, W.B. Cai, High performance Ag rich Pd-Ag bimetallic electrocatalyst for ethylene glycol oxidation in alkaline media, *J. Electrochem. Soc.* 165 (2018) J3259–J3265.
- [35] R. Bai, G. He, L. Li, T. Zhang, J. Li, X. Wang, X. Wang, Y. Zou, D. Mei, A. Corma, J. Yu, Encapsulation of palladium carbide subnanometric species in zeolite boosts highly selective semihydrogenation of alkynes, *Angew. Chem. Int. Ed.* 62 (2023) e202313101.
- [36] K. Mori, T. Sano, H. Kobayashi, H. Yamashita, Surface engineering of a supported PdAg catalyst for hydrogenation of CO<sub>2</sub> to formic acid: Elucidating the active Pd atoms in alloy nanoparticles, *J. Am. Chem. Soc.* 140 (2018) 8902–8909.
- [37] L.E. Betancourt, A. Rojas-Pérez, I. Orozco, A.I. Frenkel, Y. Li, K. Sasaki, S. D. Senanayake, C.R. Cabrera, Enhancing ORR performance of bimetallic PdAg electrocatalysts by designing interactions between Pd and Ag, *ACS Appl. Energy Mater.* 3 (2020) 2342–2349.
- [38] P. Verma, Y. Kuwahara, K. Mori, H. Yamashita, Synthesis and characterization of a Pd/Ag bimetallic nanocatalyst on SBA-15 mesoporous silica as a plasmonic catalyst, *J. Mater. Chem. A* 3 (2015) 18889–18897.
- [39] M. Navlani-García, K. Mori, A. Nozaki, Y. Kuwahara, H. Yamashita, Screening of carbon-supported PdAg nanoparticles in the hydrogen production from formic acid, *Ind. Eng. Chem. Res.* 55 (2016) 7612–7620.
- [40] C. Wang, Y. Li, C. Zhang, X. Chen, C. Liu, W. Weng, W. Shan, H. He, A simple strategy to improve Pd dispersion and enhance Pd/TiO<sub>2</sub> catalytic activity for formaldehyde oxidation: the roles of surface defects, *Appl. Catal. B-Environ.* 282 (2021) 119540.
- [41] J. Gu, S. Wang, Z. He, Y. Han, J. Zhang, Direct synthesis of hydrogen peroxide from hydrogen and oxygen over activated-carbon-supported Pd–Ag alloy catalysts, *Catal. Today* 6 (2016) 809–817.
- [42] Z. Liu, Y. An, G. Xu, Y. Yu, H. He, Insight into the promotion effect of trace Pd doping on the catalytic performance of Ag/Al<sub>2</sub>O<sub>3</sub> for C<sub>3</sub>H<sub>6</sub>-SCR of NO<sub>x</sub>, *Environ. Sci. Technol.* 57 (2023) 14760–14767.
- [43] M.E. Hernández-Terán, J.C. López Curiel, G.A. Fuentes, Study of the reversibility of the H<sub>2</sub> effect over Ag/γ-Al<sub>2</sub>O<sub>3</sub> catalyst during selective catalytic reduction (SCR) of NO<sub>x</sub> by propane, *Top. Catal.* 65 (2022) 1505–1515.
- [44] M. Richter, The effect of hydrogen on the selective catalytic reduction of NO in excess oxygen over Ag/Al<sub>2</sub>O<sub>3</sub>, *Appl. Catal. B-Environ.* 51 (2004) 261–274.
- [45] Z. Hou, Y. Liu, J. Deng, Y. Lu, S. Xie, X. Fang, H. Dai, Highly active and stable Pd–GaO<sub>x</sub>/Al<sub>2</sub>O<sub>3</sub> catalysts derived from intermetallic Pd<sub>5</sub>Ga<sub>3</sub> nanocrystals for methane combustion, *ChemCatChem* 10 (2018) 5637–5648.
- [46] M. Xiao, X. Yu, Y. Guo, M. Ge, Boosting toluene combustion by tuning electronic metal–support interactions in in situ grown Pt@Co<sub>3</sub>O<sub>4</sub> Catalysts, *Environ. Sci. Technol.* 56 (2021) 1376–1385.
- [47] W. Wang, W. Zhou, W. Li, X. Xiong, Y. Wang, K. Cheng, J. Kang, Q. Zhang, Y. Wang, In-situ confinement of ultrasmall palladium nanoparticles in silicalite-1 for methane combustion with excellent activity and hydrothermal stability, *Appl. Catal. B-Environ.* 276 (2020) 119142.
- [48] S. Tang, H. Liu, T. Li, C. Wang, Q. Cui, Y. Yue, X. Meng, X. Bao, Encapsulating platinum nanoparticles into multi-hollow silicalite-1 zeolite for catalytic oxidation of volatile organic compounds, *Chem. Eng. Sci.* 286 (2024) 119674.
- [49] Z. Wang, H. Yang, R. Liu, S. Xie, Y. Liu, H. Dai, H. Huang, J. Deng, Probing toluene catalytic removal mechanism over supported Pt nano- and single-atom-catalyst, *J. Hazard. Mater.* 392 (2020) 122258.
- [50] Y. Du, J. Zou, Y. Guo, X. Xu, H. Chen, C. Su, Z. Zeng, L. Li, A novel viewpoint on the surface adsorbed oxygen and the atom doping in the catalytic oxidation of toluene over low-Pt bimetal catalysts, *Appl. Catal.*, A. 609 (2021) 117913.
- [51] C. Wang, N. Xu, K. Huang, B. Liu, P. Zhang, G. Yang, H. Guo, P. Bai, S. Mintova, Emerging co-synthesis of dimethyl oxalate and dimethyl carbonate using Pd/silicalite-1 catalyst with synergistic interactions of Pd and silanols, *Chem. Eng. J.* 466 (2023) 143136.
- [52] Y. Pan, A. Bhowmick, W. Wu, Y. Zhang, Y. Diao, A. Zheng, C. Zhang, R. Xie, Z. Liu, J. Meng, D. Liu, Titanium silicalite-1 nanosheet-supported platinum for non-oxidative ethane dehydrogenation, *ACS Catal.* 11 (2021) 9970–9985.
- [53] F. Bi, S. Ma, B. Gao, B. Liu, Y. Huang, R. Qiao, X. Zhang, Boosting toluene deep oxidation by tuning metal-support interaction in MOF-derived Pd@ZrO<sub>2</sub> catalysts: the role of interfacial interaction between Pd and ZrO<sub>2</sub>, *Fuel* 357 (2024) 129833.
- [54] F. Rainone, D.A. Bulushev, L. Kiwi-Minsker, A. Renken, DRIFTS and transient-response study of vanadia/titania catalysts during toluene partial oxidation, *Phys. Chem. Chem. Phys.* 5 (2003) 4445–4449.
- [55] R. Mi, D. Li, Z. Hu, R.T. Yang, Morphology effects of CeO<sub>2</sub> nanomaterials on the catalytic combustion of toluene: a combined kinetics and diffuse reflectance infrared fourier transform spectroscopy study, *ACS Catal.* 11 (2021) 7876–7889.
- [56] W. Liu, S. Yang, H. Yu, S. Liu, H. Li, Z. Shen, Z. Song, X. Chen, X. Zhang, Boosting the total oxidation of toluene by regulating the reactivity of lattice oxygen species and the concentration of surface adsorbed oxygen, *Sep. Purif. Technol.* 325 (2023) 124597.
- [57] L. Wang, Y. Li, J. Liu, Z. Tian, Y. Jing, Regulation of oxygen vacancies in cobalt-cerium oxide catalyst for boosting decontamination of VOCs by catalytic oxidation, *Sep. Purif. Technol.* 277 (2021) 119505.
- [58] P. Wang, J. Wang, X. An, J. Shi, W. Shangquan, X. Hao, G. Xu, B. Tang, A. Abudula, G. Guan, Generation of abundant defects in Mn-Co mixed oxides by a facile agar-gel method for highly efficient catalysis of total toluene oxidation, *Appl. Catal. B-Environ.* 282 (2021) 119560.
- [59] S. Mo, Q. Zhang, J. Li, Y. Sun, Q. Ren, S. Zou, Q. Zhang, J. Lu, M. Fu, D. Mo, J. Wu, H. Huang, D. Ye, Highly efficient mesoporous MnO<sub>2</sub> catalysts for the total toluene oxidation: oxygen-Vacancy defect engineering and involved intermediates using in situ DRIFTS, *Appl. Catal. B-Environ.* 264 (2020) 118464.
- [60] Y. Shen, J. Deng, S. Impeng, S. Li, T. Yan, J. Zhang, L. Shi, D. Zhang, Boosting toluene combustion by engineering Co–O strength in cobalt oxide catalysts, *Environ. Sci. Technol.* 54 (2020) 10342–10350.